Heliyon 9 (2023) e20902

Contents lists available at ScienceDirect

Heliyon

journal homepage: www.cell.com/heliyon

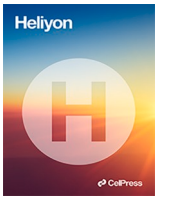

Physics-based and data-driven modeling for basal stability evaluation of braced excavations in natural clays

Van Qui Lai [a,b], Khamnoy Kounlavong [c], Suraparb Keawsawasvong [c], Warit Wipulanusat [d,*], Pitthaya Jamsawang [e]

[a] Faculty of Civil Engineering, Ho Chi Minh City University of Technology (HCMUT), 268 Ly Thuong Kiet Street, District 10, Ho Chi Minh City, Viet Nam
[b] Vietnam National University Ho Chi Minh City (VNU–HCM), Linh Trung Ward, Thu Duc District, Ho Chi Minh, City, Viet Nam
[c] Research Unit in Sciences and Innovative Technologies for Civil Engineering Infrastructures, Department of Civil Engineering, Faculty of Engineering, Thammasat School of Engineering, Thammasat University, Pathumthani, 12120, Thailand
[d] Research Unit in Data Science and Digital Transformation, Department of Civil Engineering, Faculty of Engineering, Thammasat School of Engineering, Thammasat University, Pathumthani, 12120, Thailand
[e] Soil Engineering Research Center, Department of Civil Engineering, King Mongkut's University of Technology North Bangkok, Bangkok, 10800, Thailand

ARTICLE INFO

Keywords:
Basal stability
Plane strain excavation
Anisotropy
ANN
FELA

ABSTRACT

The design of fully braced excavation of underground works, whether in rural or urban areas, is important to ensure that the design of fully braced support is safe, particularly in determining the depth of excavation and inserting the length into the clay of the wall, as well as a proportional excavation width. This study investigates the undrained basal stability of fully braced excavation in anisotropic clays with linearly increasing shear strength with depth employing upper and lower bound finite element limit analysis under symmetry plane conditions based on the AUS failure criterion. The dimensionless variables were used to examine the stability number (N) and the failure mechanisms selected for this problem's practical analysis. There is an anisotropic strength ratio (r_e), depth-wide ratio (B/H), embedded wall depth ratio (D/H), and strength gradient factor ($\rho H/S_{uc0}$). This study proposes design charts and failure mechanisms for fully braced excavations based on finite element limit analysis. Moreover, the artificial neural network model (ANN) was used to establish the relationship between the investigated and output variables and to conduct sensitivity analysis. Therefore, the developed ANN formula is a pragmatic approach for geotechnical engineers to calculate the basal stability of the excavations.

1. Introduction

Generally, natural clay partial strength anisotropy emanates from depositional and sedimentation processes, resulting in a particular particle orientation [1]. The shear strength anisotropy of clays is directional (i.e., depending on the depositional direction). Three anisotropic undrained shear strengths can be obtained through triaxial compression, triaxial extension, and direct simple shear tests, which are defined as S_{uc}, S_{ue}, and S_{us}, respectively. To take this phenomenon into account, Krabbenhøft et al. [2] recently proposed the anisotropic undrained shear (AUS) model extending from the Generalized Tresca model to anisotropic materials,

* Corresponding author.
E-mail address: wwarit@engr.tu.ac.th (W. Wipulanusat).

https://doi.org/10.1016/j.heliyon.2023.e20902
Received 16 May 2023; Received in revised form 8 October 2023; Accepted 10 October 2023
Available online 12 October 2023

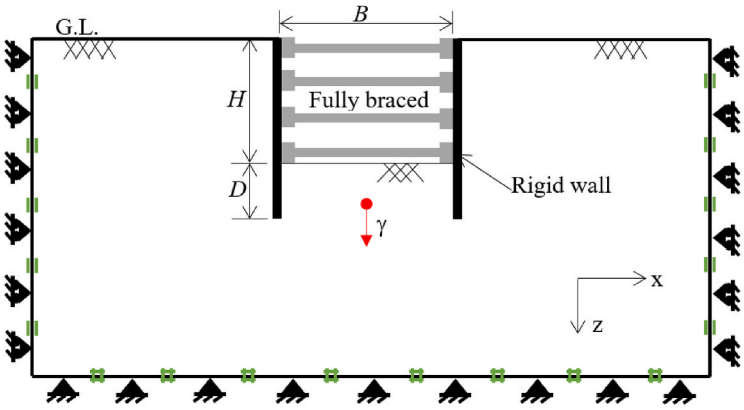

(a) Model of the fully braced excavation

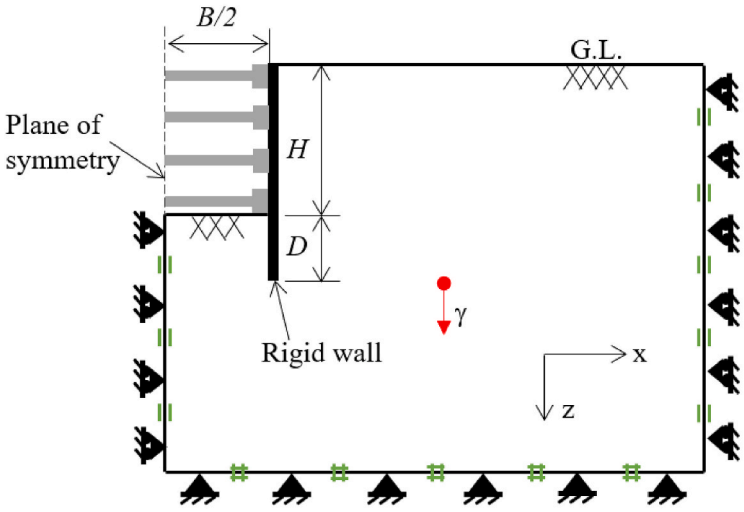

(b) Model of the half-braced excavation

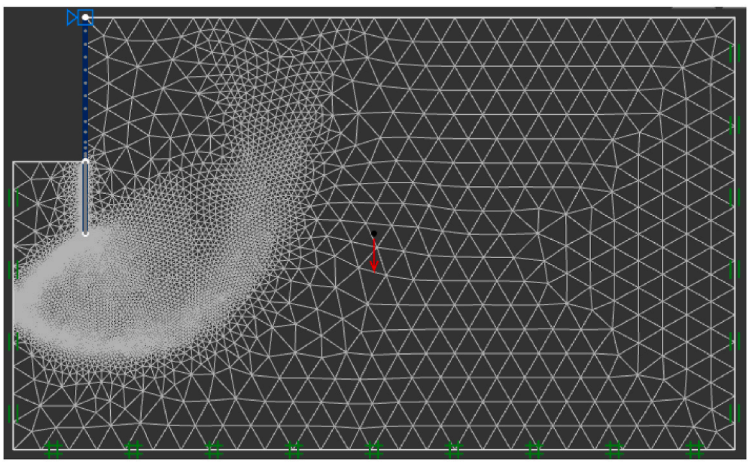

(c) Final adaptive meshes

Fig. 1. Problem definition of the rigid wall fully braced excavation in plane strain condition; where (a) Model of the fully braced excavation, (b) Model of the half-braced excavation, and (c) Final adaptive meshes.

specifically regarding the case of cross anisotropy (or transversely isotropic materials). Several researchers have employed the application of the AUS model in conjunction with finite element limit analysis (FELA) to successfully compute the stability solutions for various geotechnical issues, for instance, the bearing capacity of footings [e.g. Refs. [3–6]], the pullout capacity of caissons or anchors [e.g. Refs. [7–9]], the slope stability [e.g. Ref. [10]], the stability of unsupported excavations [e.g. Refs. [11–13]], and the problem of the limiting pressure behind soil gaps or trapdoors [e.g. Refs. [14–16]].

Due to the worldwide limitation of surface spaces in megacities caused by increased population and rural-to-urban migration, the use of underground spaces has increased. As a result, the number of diaphragm walls or piled wall constructions of basements and deep foundations has increased. However, previous research has focused on the serviceability aspect of wall movements and lateral earth pressures related to stresses around excavated areas (e.g. Refs. [17–34]). Nevertheless, there have been few studies on braced excavations' basal heave stability.

Terzaghi [35] and Bjerrum and Eide [36] originally introduced analytical methods for computing solutions for braced excavations' basal heave stability by employing the limit equilibrium method (LEM). In their methods, the assumptions of the basal heave problem's failure pattern were carried out to produce the limit equilibrium equations for calculating the factor of safety. Later, Goh [37,38] and Faheem et al. [39] employed the displacement–based finite element method (DB-FEM) to solve the plane strain excavations' basal heave stability. The finite element limit analysis (FELA) was also used by Yodsomjai et al. [40] to obtain plastic bound solutions to the same problem. Moreover, the basal heave stability of braced circular excavations was also investigated by Cai et al. [41], Goh [42], and Keawsawasvong and Ukritchon [43]. In the past, there were some previous studies regarding braced excavations in anisotropic clays in terms of stability and movement [44–46]. However, anisotropic and nonhomogenous clays conforming to the AUS model have never been considered for the basal heave stability problem under plane strain conditions.

The lower bound (LB) and upper bound (UB) FELA software, namely OptumG2 [47], together with the AUS model, is employed in this study to compute the basal stability solutions for plane strain excavations. The previous works by Terzaghi [35] and Bjerrum and Eide [36] employed the limit equilibrium method (LEM) in their analysis, where the simple patterns of the failure lines around excavations were assumed before computing. In addition, Goh [37,38] and Faheem et al. [39] carried out solutions from DB-FEM models with very coarse mesh distributions indicating an insufficient number of meshes in their FEA models. However, this study used the FELA with the mesh adaptivity approach to obtain more accurate limit state solutions of the excavation problem. Note that the fully braced supports are applied to the wall, indicating that there is no horizontal movement or rotation of the wall. Since the AUS model is adopted as a failure criterion of anisotropic clays, two anisotropic strength ratios are proposed: $r_e = S_{ue}/S_{uc}$ and $r_s = S_{us}/S_{uc}$ to normalize those three anisotropic undrained shear strength components. It is worth noting that the relationship of r_e and r_s can be computed from $r_s = 2r_e/(1+r_e)$ and the range of r_e varying from 0.5 to 1. When $r_e = 1$, the case of isotropic undrained shear strength can be simulated. The non-homogenous properties of clays are also considered in this study. A non-homogeneous clay's undrained shear strength profile is a linear function of $S_{uc}(z) = S_{uc0} + \rho z$, where S_{uc0} represents a surface undrained shear strength and ρ denotes a strength gradient. After obtaining the UB and LB solutions to the plane strain excavation problem, the artificial neural network (ANN) model is used to formulate the relationship between the investigated and output variables and conduct sensitivity analysis. The proposed formula can be effective for practical engineering in directly estimating the investigated stability number. Furthermore, sensitivity analysis is useful for selecting the value of input parameters in the initial stage.

2. Method of analysis

This paper utilizes the finite element limit analysis, OptumG2 software [47], to compute rigorous UB and LB solutions on collapse loads of fully braced excavation in plane strain conditions. OptumG2 is FELA software that was developed based on a numerical technique with the limit analysis theory used in structural and geotechnical engineering to evaluate the ultimate strength or collapse load-carrying capacity of a structure or soil mass. The process in OptumG2 involves performing an iterative optimization algorithm on the finite element mesh to find the load distribution that results in the highest factor of safety or critical load factor. The critical load factor represents the ratio of the applied load to the ultimate load capacity of the structure. By combining the accuracy and versatility of finite element analysis with rigorous limit analysis principles, FELA can efficiently analyze complex structures and geotechnical problems to predict their ultimate load-carrying capacity.

As shown in Fig. 1(a), the excavation has a width of B, a depth of H, and a wall embedment of D. Due to the symmetry of the problem, only half the domain can be used in the simulation, as shown in Fig. 1(b). Additionally, the features of all numerical model boundaries imposed that the left and right boundaries can move only in the vertical direction. The bottom ones have no movements in either the vertical or horizontal axis. In addition, the wall is modeled as a rigid plate with no failure prior to the soil's collapse. Both the unit weight supports and walls are neglected, and it is assumed that the interface between the wall and the clay is rough. To avoid the impact of the weight of the wall on the computed results, this study ignores this weight term by only focusing on the weight of the soil mass behind the wall. Note that the roughness of the wall can be varied from fully smoother to rough. However, this study considers only the rough case. Future works are requested to further investigate the impact of wall roughness.

Very fine-meshed elements and three iterations of numerical analyses are applied to obtain accurate results for UB and LB solutions, along with adaptivity control shear dissipation. The adaptive meshing process can be summarized as follows:

Initialization: The user specifies the initial number of elements, which defines the mesh size distribution.

Step 1. A mesh is generated based on the specified mesh size distribution.

Step 2. The limit analysis problem is solved using finite element discretizations applied to the mesh created in Step 1. If the number of adaptive iterations exceeds the predefined limit, the adaptivity loop is considered complete. If not, the process continues to Step 3.

Step 3. An optimum adaptive technique is employed to update the mesh size distribution based on the adaptivity control shear dissipation. After this, the process returns to Step 1 for the next iteration.

In summary, adaptive meshing proceeds by creating an initial mesh, solving the problem on that mesh, and then updating the mesh size distribution iteratively until the desired level of accuracy is achieved. The mesh element number used in this study starts from 5000 to 10,000 elements at the final step. The automatic mesh element development in the numerical modeling of a braced excavation by OptumG2 software has finer mesh at the bottom of wall regions, as shown in Fig. 1(c). Moreover, it will become coarser when the distance of the excavation model edge increases. Note that the sizes of the domains for all models are set to be large enough so that there is no intersection of the failure lines to the right and bottom boundaries to maintain the correctness of the limit state solution using FELA.

In this paper, the output from FELA is the maximum unit weight (γ) that causes the basal heave failure of the planar excavations. The input parameters are used to analyze the UB and LB undrained stability of fully braced excavation in non-homogeneous and anisotropic clays to obtain the stability number that can be adopted to calculate the maximum unit weight depending on these variables, consisting of H, D, B, S_{uc0}, ρ, and r_e ($= S_{ue0}/S_{uc0}$). The dimensionless technique was used to simplify the investigated variables of four dimensionless input parameters and to derive the stability solutions in terms of the stability number ($N = \gamma H/S_{uc0}$). These parameters can be shown for correlation of the fully braced excavation's stability number as follows:

$$N = \frac{\gamma H}{S_{uc0}} \propto f\left(\frac{B}{H}, \frac{D}{H}, \frac{\rho H}{S_{uc0}}, r_e\right) \tag{1}$$

where:

B/H is the depth-width ratio.

D/H is the depth ratio of the embedded wall

$\rho H/S_{uc0}$ is the strength gradient factor

r_e is an anisotropic strength ratio.

N is the stability number of the fully braced excavation.

Eq. (1) is expressed in this paper to demonstrate the relationship between four dimensionless inputs and one dimensionless output. The parametric studies and their ranges that are used to model and analyze the solutions of UB and LB finite element limit analysis of fully braced excavation in plane strain conditions consist of $D/H = 0$–1, $B/H = 0.25$–2, $\rho H/S_{uc0} = 0$–4, and $r_e = 0.5$–1. These values are shown in Table 1. The ranges of these parametric studies are referred from previous works conducted by Refs. [40,43]. Note that the factor of safety (FS) can be included in the stability by $N = \gamma H/S_{uc0} = \gamma H(FS)/S_{uci}$, where S_{uci} is the undrained shear strength from the compression test that is obtained in the field before the excavation collapse and S_{uc0} is the reduced undrained shear strength at the collapse ($S_{uc0} = S_{uc0i}/FS$).

3. Results and discussion

The mean value of the UB and LB FELA solutions for the stability numbers of current fully braced excavation results are compared with the previous results by Yodsomjai et al. [40], using the finite element limit analysis, OptumG2 software [47], where the soil properties used for the analysis of this stability number (N) of fully braced excavation were modeled as an AUS material model, while the previous studies modeled the soil properties as Tresca material.

It is recognized that verifying the numerical model is the most crucial thing before further analysis. Therefore, Fig. 2 is prepared between the present study and previous results from Yodsomjai et al. [47] for the case of isotropic ($r_e = 1$) and non-homogeneous clays. By setting the parameter r_e to one, the mathematical function of the AUS model can approximately become the Tresca model. Furthermore, Fig. 2 also represents the function of the correlation between the depth ratio of the embedded wall (D/H) and the stability number of fully braced excavation (N), which has functions of the strength gradient factors $\rho H/S_{uc0}$, depth-width ratio B/H, and isotropic strength ratio r_e. From the results in Fig. 2, it can be concluded that this study's results have values greater than the previous studies' results in all cases of $\rho H/S_{uc0}$. As proposed above, the values of N from the AUS model were not equal to those from the Tresca model because of the mathematical function of the flow rules between both models. Consequently, the N value obtained from the present study differs from the previous study by Yodsomjai et al. [47] using the Tresca failure criterion.

Fig. 3(a–d) presents the correlation between N and $\rho H/S_{uc0}$ for the case of an anisotropic clay with $r_e = 0.5$. The dimensionless parameters selected to examine this problem consist of four parameters, namely, B/H, D/H, r_e, and $\rho H/S_{uc0}$. Examining the results in Fig. 3a–d, the value of N increases with an increase in the $\rho H/S_{uc0}$ and D/H ratios, and the tendency of N is linear in all cases of D/H ratios. On the other hand, the N factor decreases when the B/H ratio increases. Based on the preceding findings, we can deduce that

Table 1
The input data range.

Parameters	Input values	Max	Mean	Min
B/H	0.25, 0.5, 1, 2	2	0.938	0.25
r_e	0.5, 0.6, 0.7, 0.8, 0.9, 1.	1	0.75	0.5
$\rho H/S_{uc0}$	0, 1, 2, 3, 4	4	2	0
D/H	0, 0.25, 0.5, 0.75, 1	1	0.5	0

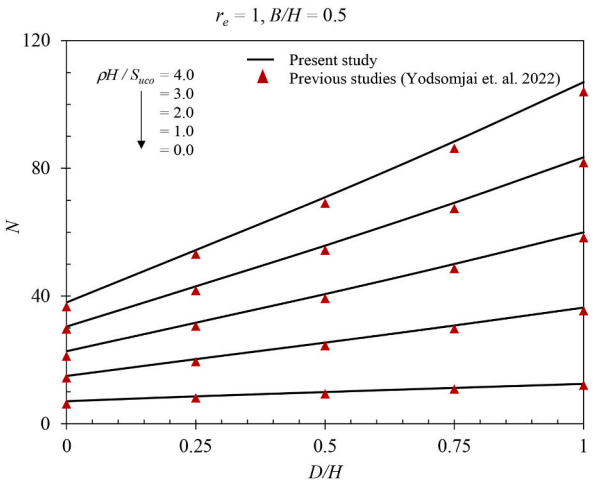

Fig. 2. Comparison between the present study and the previous study's results from Yodsomjai et al. [47].

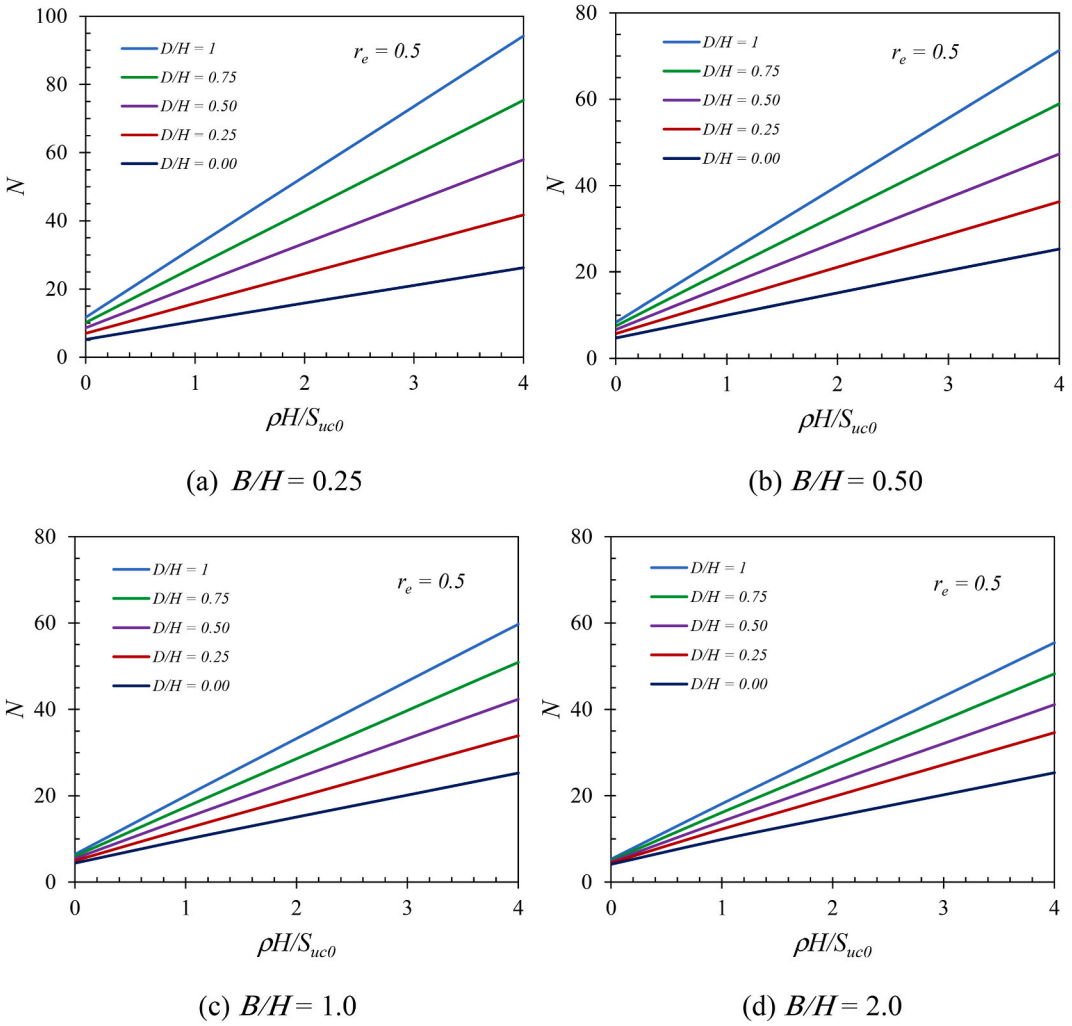

Fig. 3. Correlation between N and $\rho H/S_{uc0}$ ratios of the fully braced excavation in plane strain conditions, where r_e = 0.5; B/H = 0.25, 0.50, 1.0, 2.0; D/H = 0, 0.25, 0.50, 0.75, 1.0; and $\rho H/S_{uc0}$ = 0, 1, 2, 3, 4.

when the strength gradian factor ($\rho H/S_{uc0}$) has a significant ratio value, the soil shear strength increases with that ratio value. Therefore, the soil strength will increase with depth as an $\rho H/S_{uc0}$ increases, which means that the soil can support its own weight more effectively than in the case of a small $\rho H/S_{uc0}$ ratio value. The correlations between $\rho H/S_{uc0}$ and N are also shown in Fig. 4(a–d), Fig. 5 (a–d), Fig. 6(a–d), Fig. 7(a–d), and Fig. 8(a–d), for the different values of $r_e = 0.6$, 0.7, 0.8, 0.9, and 1, respectively. It can be observed from Fig. 4(a) to 8(d) that all of the increasing trend lines of the N value are similar to Fig. 3(a–d), which are linear. The results shown in Fig. 3(a)–8(b) can be used as the design charts for evaluating the stability of fully supported excavations in anisotropic and isotropic clays considering the linear increase in soil strength with depth.

To demonstrate the impacts of other parameters, in addition to the correlation of N with $\rho H/S_{uc0}$, the correlations between N and other dimensionless variables, namely, D/H, B/H, and r_e are shown in Figs. 9–11. Fig. 9(a) and (b) indicate the correlation between D/H and N for narrow and broad fully braced supported excavations ($B/H = 0.25$ and 1), where $r_e = 0.5$. The dimensionless parameters are selected to investigate the influence of D/H on N comprising $D/H = 0$ and $\rho H/S_{uc0} = 0$ to 4. From the results in those figures, it can be seen that N increases as both the D/H and $\rho H/S_{uc0}$ ratios increase. When the length of the clay-embedded portion of the wall is sufficient, the D/H ratio is an important dimensionless parameter. It will help the wall resist the forces transferred from the soil's weight to the wall as we excavate the soil.

Fig. 10(a and b) demonstrates the influence of B/H on N for both cases of no embedded wall (Fig. 10(a)) and an embedded wall case (Fig. 10(b)). The dimensionless variables selected to examine the effect of B/H on N consist of D/H, r_e, and $\rho H/S_{uc0}$. These dimensionless variables are equal to $D/H = 0$ and 1; $r_e = 0.5$; and $\rho H/S_{uc0} = 0$ to 4. From the overall observation, the influence of B/H on N can be divided into three terms. First, in terms of no embedded wall ($D/H = 0$) with narrow excavation ($B/H = 0.25$ and 0.5), the N value decreases when the B/H ratio increases for the cases of $\rho H/S_{uc0} = 0$ to 4. Second, in terms of no embedded wall ($D/H = 0$) with broad excavation ($B/H = 1$ and 2), the N value does not change even though B/H increases for the cases of $\rho H/S_{uc0} = 1$ to 4. For

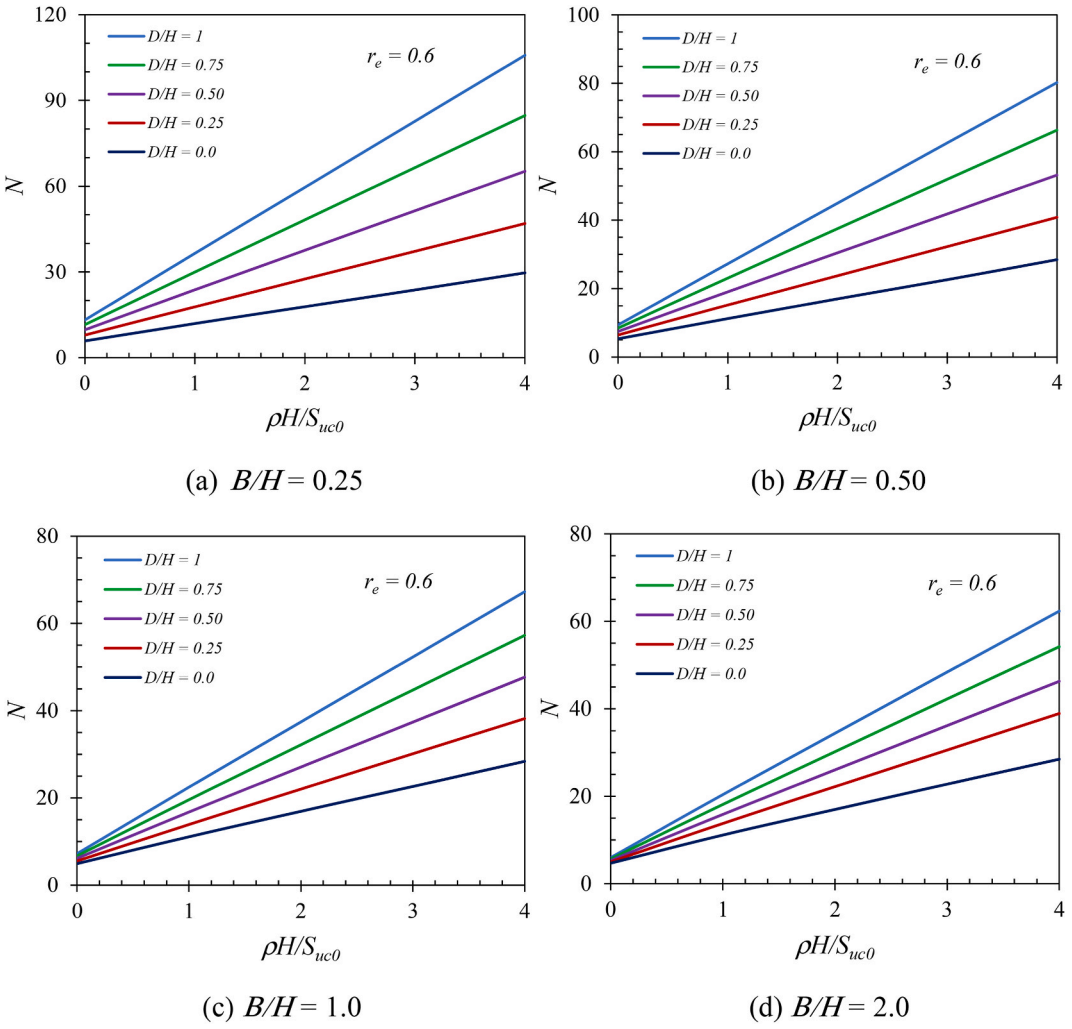

Fig. 4. Correlation between N and $\rho H/S_{uc0}$ ratios of the fully braced excavation in plane strain conditions, where $r_e = 0.6$; $B/H = 0.25$, 0.50, 1.0, 2.0; $D/H = 0$, 0.25, 0.50, 0.75, 1.0; and $\rho H/S_{uc0} = 0$, 1, 2, 3, 4.

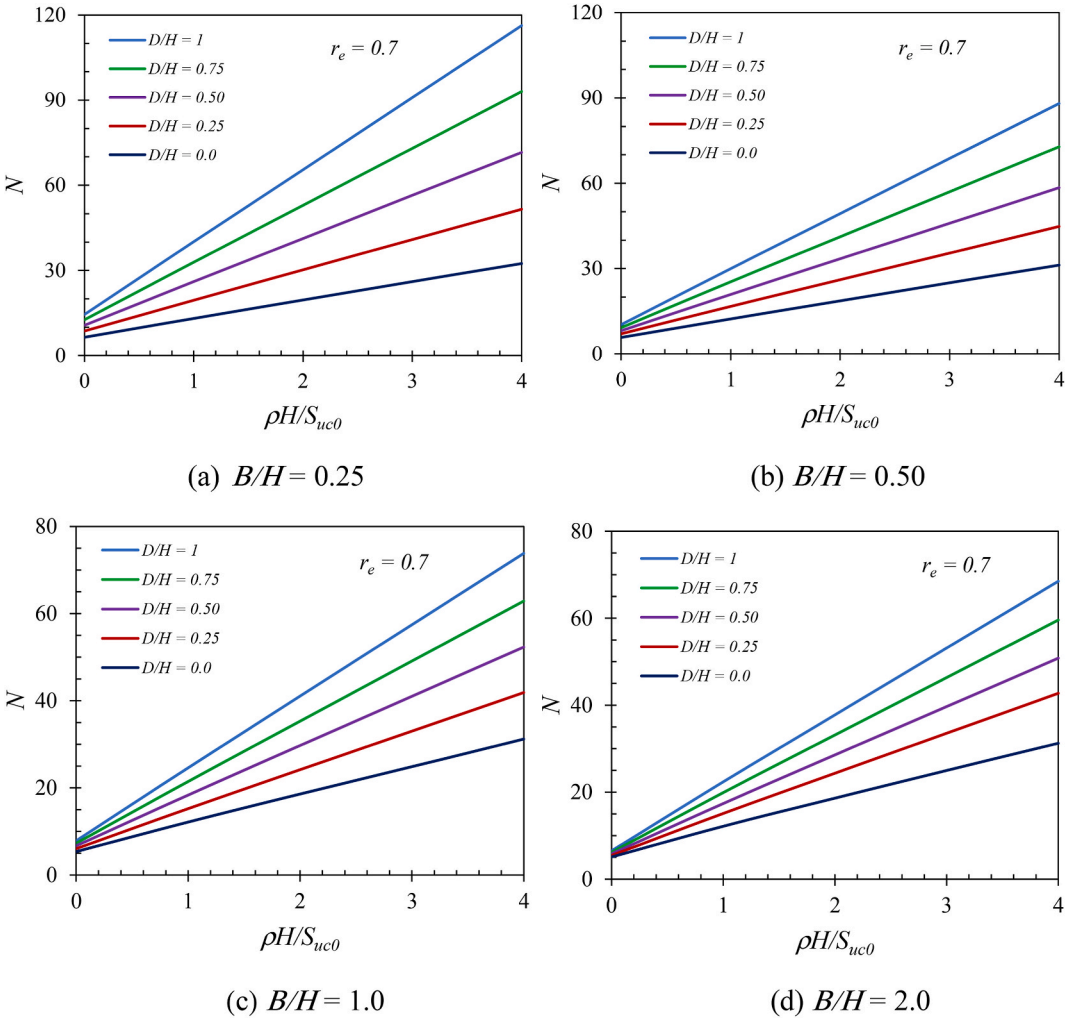

Fig. 5. Correlation between N and $\rho H/S_{uc0}$ ratios of the fully braced excavation in plane strain conditions, where $r_e = 0.7$; $B/H = 0.25$, 0.50, 1.0, 2.0; $D/H = 0$, 0.25, 0.50, 0.75, 1.0; and $\rho H/S_{uc0} = 0$, 1, 2, 3, 4.

example, in the case of $D/H = 0$, $r_e = 0.5$, $\rho H/S_{uc0} = 1$, and $B/H = 1$ and 2, the values of N are equal to 9.87 and 9.87 (see Fig. 10(a)). Third, in the case of an embedded wall ($D/H = 1$), N decreases when the B/H ratio increases for all cases of $\rho H/S_{uc0}$. There is no constant part in the third term. According to the findings, the influence of B/H on the N value can be summarized by stating that it does not affect the N value in the case of broad excavation and no embedded length of the wall. However, a narrow excavation with an embedded length can significantly cause a change in the N value.

Fig. 11(a and b) shows the effect of r_e on the N value for both cases of narrow and broad excavation ($B/H = 0.25$ and 1) for the case of no embedded wall ($D/H = 0$). The dimensionless variables utilized for numerical investigation in Fig. 11 to examine the influence of r_e on N consist of $r_e = 0.5$ and $\rho H/S_{uc0} = 0$ to 4. From the results, as shown in Fig. 11(a)–(b), the N value increases with an increase in both dimensionless parameters of r_e and $\rho H/S_{uc0}$ ratios for all cases, and the tendency of N is slightly non-linear for all cases of $\rho H/S_{uc0}$. As the r_e ratio increases, the parameter of S_{ue0} (undrained shear strength from the extension test) also increases while the value of S_{uc0} remains constant. Suppose S_{ue0} has a significant value up to one hundred percent or $S_{ue0} = S_{uc0} = S_{us0}$; this indicates that the soil is in an isotropic condition and can receive the same force in all directions (in the case of $r_e = 1$). As a result, the soil capacity would increase.

The dimensionless parameters used to examine the influence of the shear dissipation failure mechanisms of braced excavations consist of D/H, B/H, $\rho H/S_{uc0}$, and r_e. Fig. 12(a–e) indicates the shear dissipation failure mechanisms in the case of broad excavation ($B/H = 1$) and the soil modeled as anisotropic clay ($r_e = 0.8$) with the strength gradient factor ($\rho H/S_{uc0} = 1$). In all cases where D/H is increased, the failure mechanism zone becomes deeper and spreads upward to the wall behind. The shear dissipation failure mechanisms formed in the case of no embedded wall ($D/H = 0$) have two overlapping spiral patterns. In this instance, the most sensitive zone is beneath the excavation zone. In the case of a very shallow inserted wall ($D/H = 0.25$), the formed shear dissipation has a single spiral pattern, and a portion of the sensitive zone remains beneath the excavation. In other cases, $D/H = 0.5$, 0.75, and 1, shear

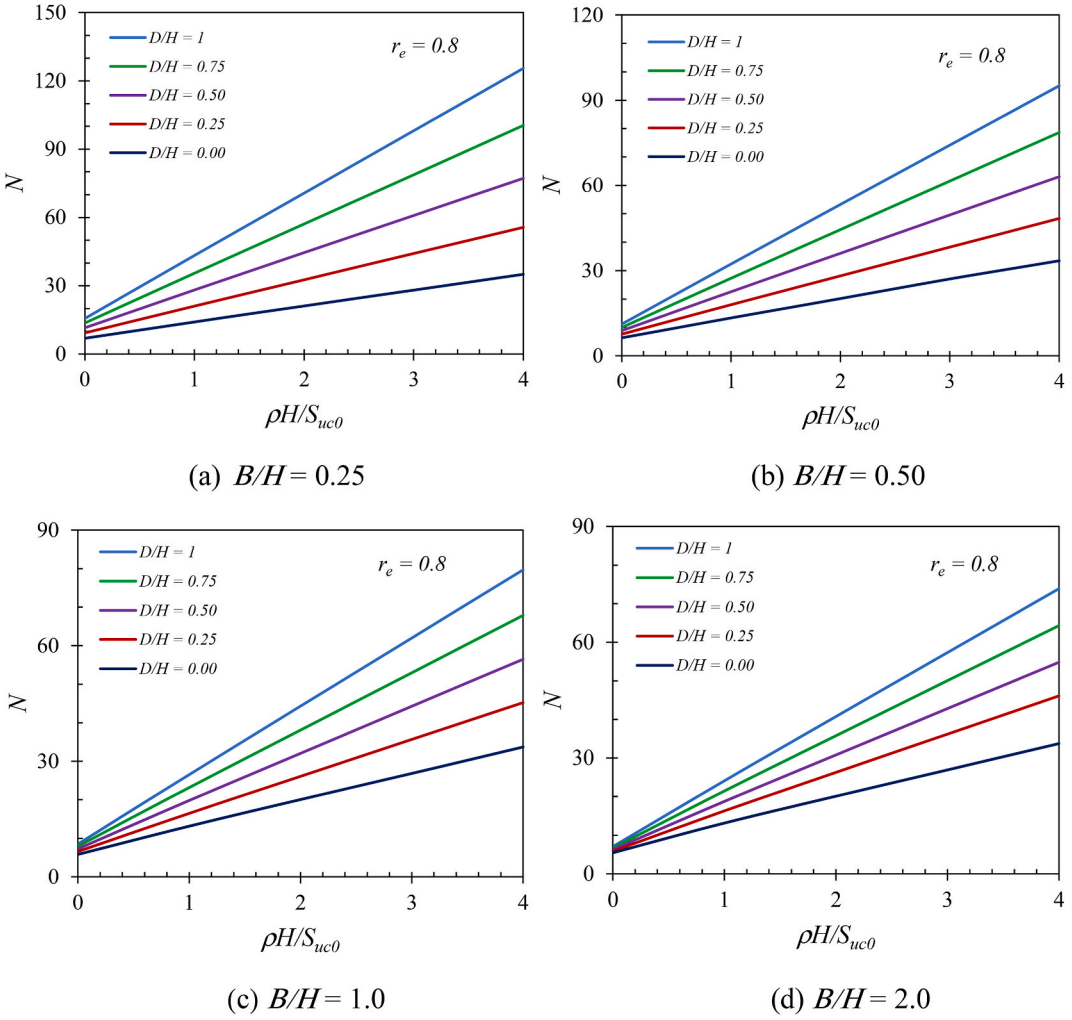

Fig. 6. Correlation between N and $\rho H/S_{uc0}$ ratios of the fully braced excavation in plane strain conditions, where $r_e = 0.8$; $B/H = 0.25$, 0.50, 1.0, 2.0; $D/H = 0$, 0.25, 0.50, 0.75, 1.0; and $\rho H/S_{uc0} = 0$, 1, 2, 3, 4.

dissipation appears as a spiral pattern. It clearly occurs at the end of the wall, cutting through to the symmetry plane under the excavated area and then extending from the base upward to the wall's right-side zone. The shear dissipation failure mechanisms described above can be explained using two terms. No embedded to shallow embedded walls or medium to deeply embedded walls exhibit distinctive shear dissipation patterns. In the no embedded to shallow embedded wall cases, the soil beneath the excavation has risen due to the downward pressure generated by the soil weight from the walls behind. At the bottom of the cut, this pressure causes a bulge. In the case of medium to deeply embedded walls, the downward pressure generated by the soil's weight cannot pass through under the bottom of the cut because the part inserted into the clay of the wall is long enough. Consequently, the shear dissipation failure mechanism occurred at the end of the bottom of the wall.

Fig. 13(a–d) shows the influence of the *B/H ratios* on the shear dissipation failure mechanisms of this issue with $D/H = 0.5$, $r_e = 0.8$, and $\rho H/S_{uc0} = 1$. In all cases, the pattern of shear dissipation changed as the B/H ratios increased. At the bottom of the cut, the failure mechanism of the wide-area excavation ($B/H = 2$) case changes significantly. The downward pressure created by the soil's weight from the walls behind was most noticeable under the excavation and along the side of the wall.

Fig. 14(a–e) demonstrates the effect of $\rho H/S_{uc0}$ on the shear dissipation failure mechanisms of this issue with $D/H = 0.5$, $r_e = 0.8$, and $B/H = 1$. The area of shear dissipation failure mechanisms decreased when the $\rho H/S_{uc0}$ ratios increased, and the failure patterns were the same spiral pattern. Except for $\rho H/S_{uc0} = 0$, the failure mechanism is half of a V-shaped pattern. Fig. 15(a–f) depicts the impact of the r_e ratio on the shear dissipation failure mechanism of fully braced excavation with $D/H = 0.5$, $\rho H/S_{uc0} = 1$, and $B/H = 1$. All failure patterns exhibit the same spiral formation, and the failure zone remains unchanged despite the increase in the r_e ratio.

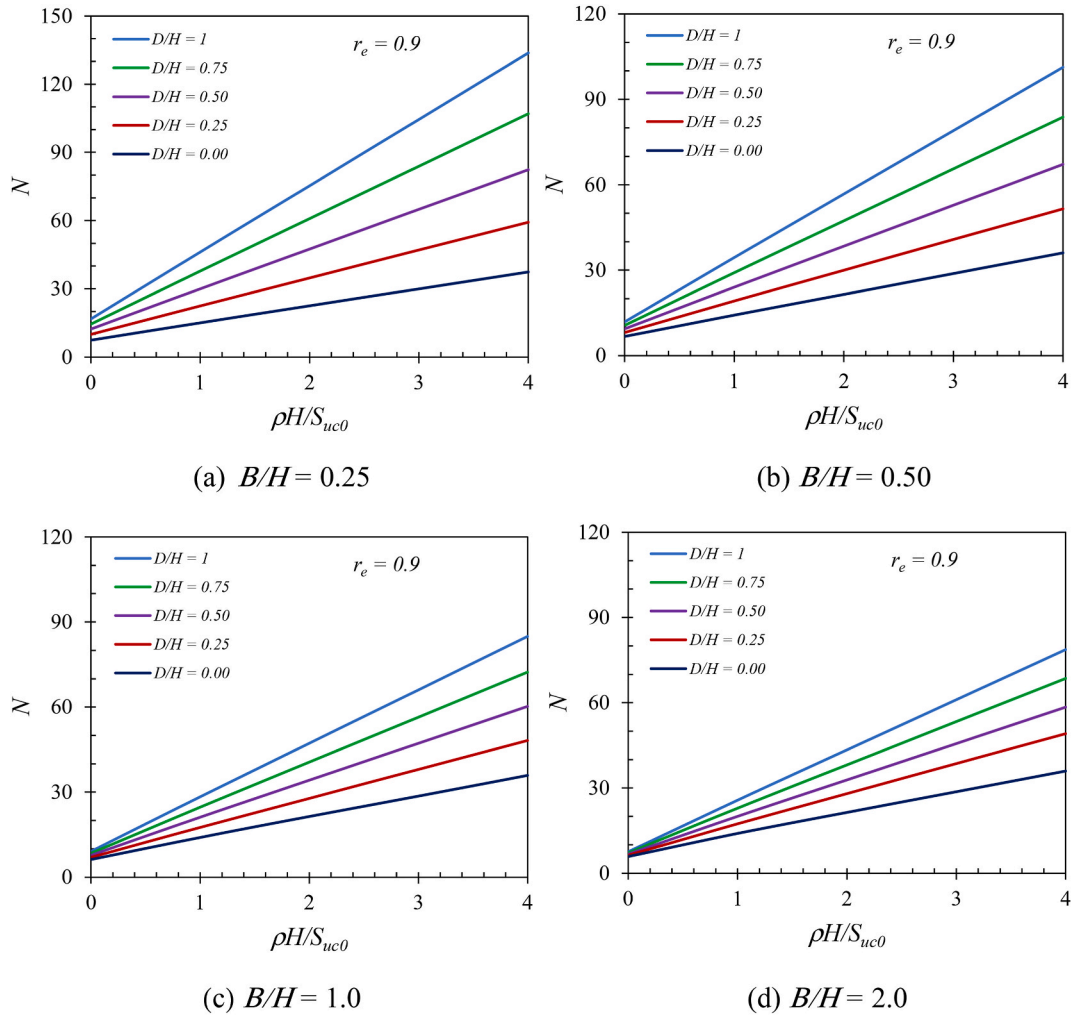

Fig. 7. Correlation between N and $\rho H/S_{uc0}$ ratios of the fully braced excavation in plane strain conditions, where $r_e = 0.9$; $B/H = 0.25$, 0.50, 1.0, 2.0; $D/H = 0$, 0.25, 0.50, 0.75, 1.0; and $\rho H/S_{uc0} = 0$, 1, 2, 3, 4.

4. ANN application

This study employs an artificial neural network (ANN) model to propose a correlation equation between the investigated input and output variables to assist practitioners in applying the findings of this paper to design work. Although the application of the ANN model appeared in the last decade and other machine learning approaches, such as MARS, RF, XGBoost, and SVM, it is still an effective approach to calibrating the complicated relationship of all parameters. The use of ANN models is more popular, which can be observed from some recent studies related to the fields of structure engineering [48,49], construction management [50], environmental engineering [51], and geotechnical engineering [52–67]. Furthermore, ANNs can be used to implement sensitivity analysis [65].

The concept of the ANN model is to emulate the functioning of the human brain by imitating its input, hidden, and output layers and their connected neurons, or nodes, as shown in Fig. 16. The current nodes are responsible for processing and transmitting input signals to the nodes that follow them. The characteristics of a neuron are expressed through the connection weight and bias constant, which are changed during learning processing. Based on the connection weight and bias of neurons, the complex nonlinear relationship between input and output variables can be simulated in terms of the tansig function [65], as presented in Eq. (2), while the impacts of input variables on the output variables, also known as sensitivity analysis, can be determined using the relative index (RI) derived from Eq. (3) [65].

$$\mathrm{N}^{predicted} = \sum_{=1}^{N_h} W^{ho}\mathrm{tansig}\left(\sum_{=1}^{Nx} W^{ih}x + b^{ih}\right) + b^{ho} \tag{2}$$

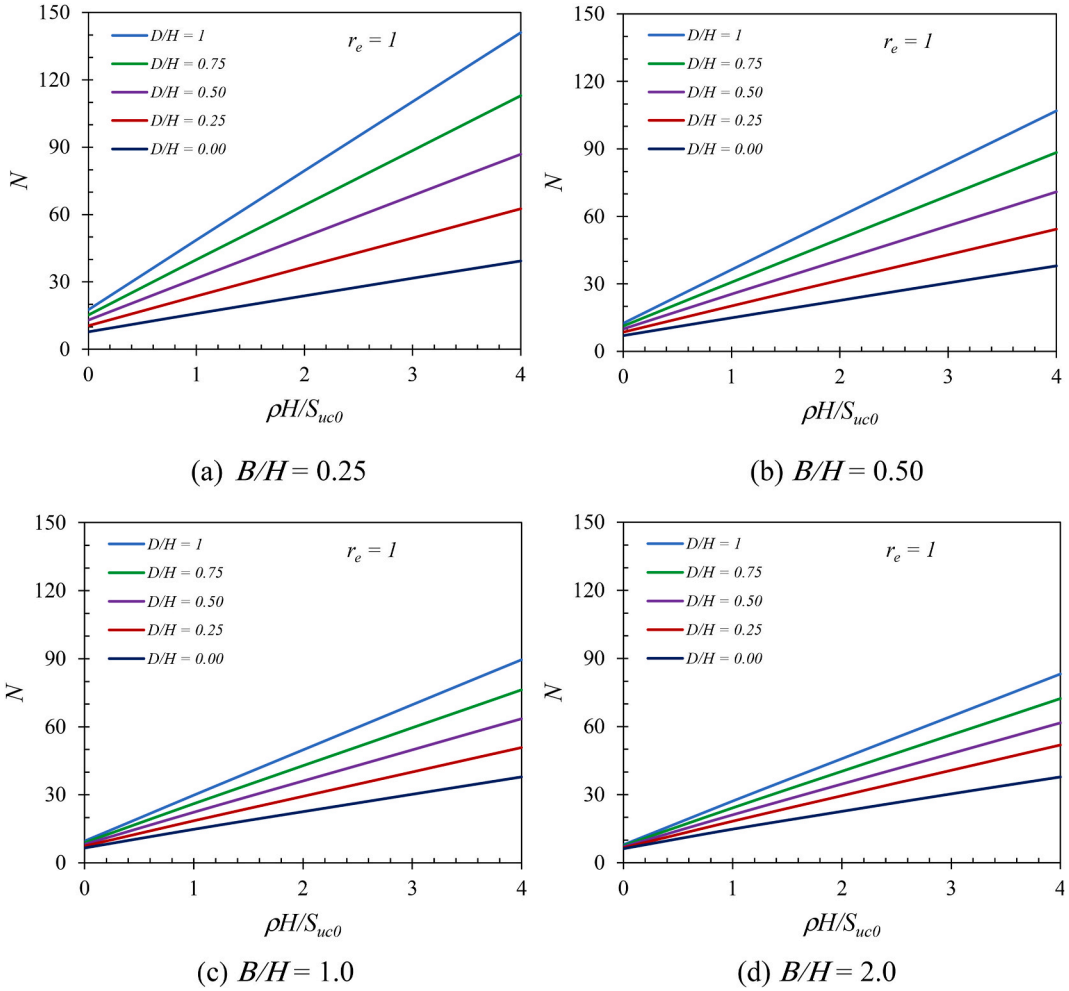

Fig. 8. Correlation between N and $\rho H/S_{uc0}$ ratios of the fully braced excavation in plane strain conditions, where $r_e = 1$; $B/H = 0.25, 0.50, 1.0, 2.0$; $D/H = 0, 0.25, 0.50, 0.75, 1.0$; and $\rho H/S_{uc0} = 0, 1, 2, 3, 4$.

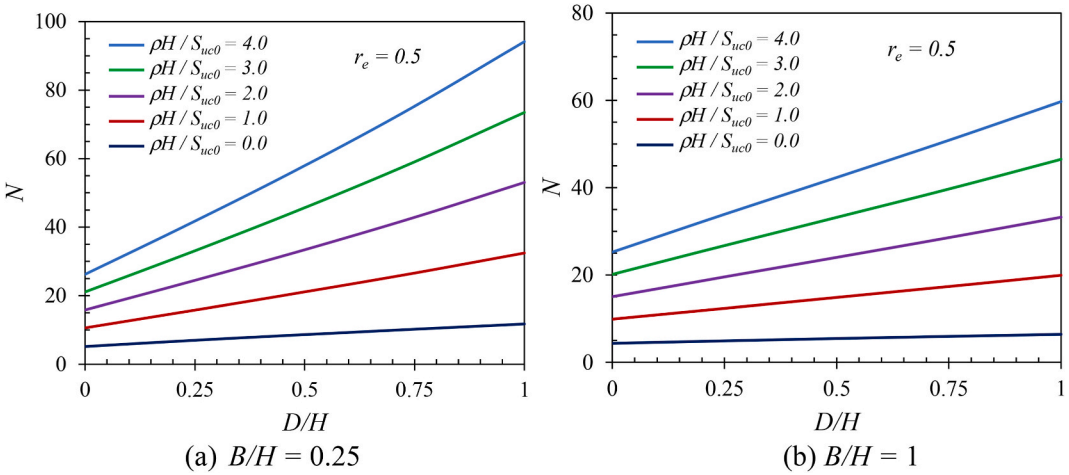

Fig. 9. Effect of the D/H on the N, where $r_e = 0.5$; $B/H = 0.25, 1$; $\rho H/S_{uc0} = 0, 1, 2, 3, 4$; and $D/H = 0, 0.25, 0.5, 0.75, 1$.

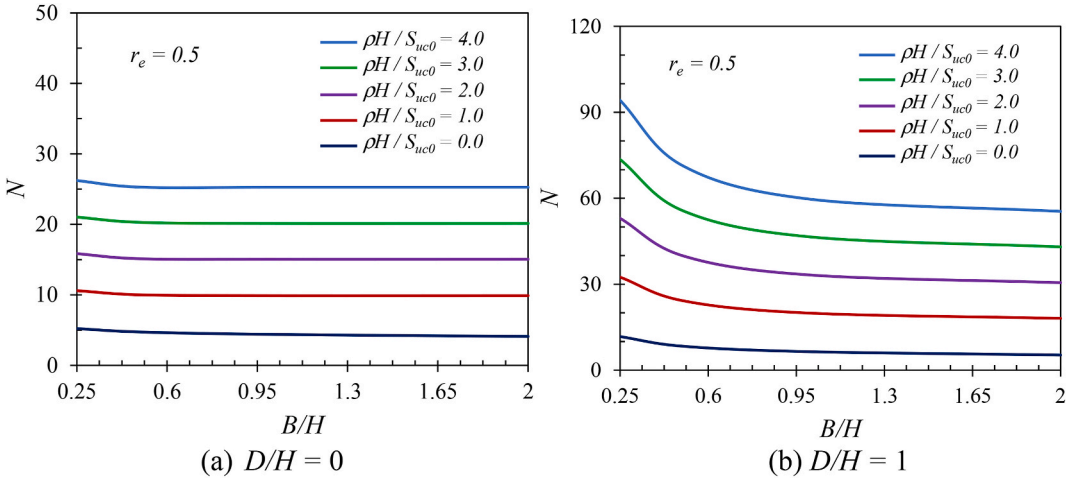

Fig. 10. Effect of the B/H on the N, where $r_e = 0.5$; $D/H = 0$, 1; $\rho H/S_{uc0} = 0$, 1, 2, 3, 4; and $B/H = 0.25$, 0.5, 1, 2.

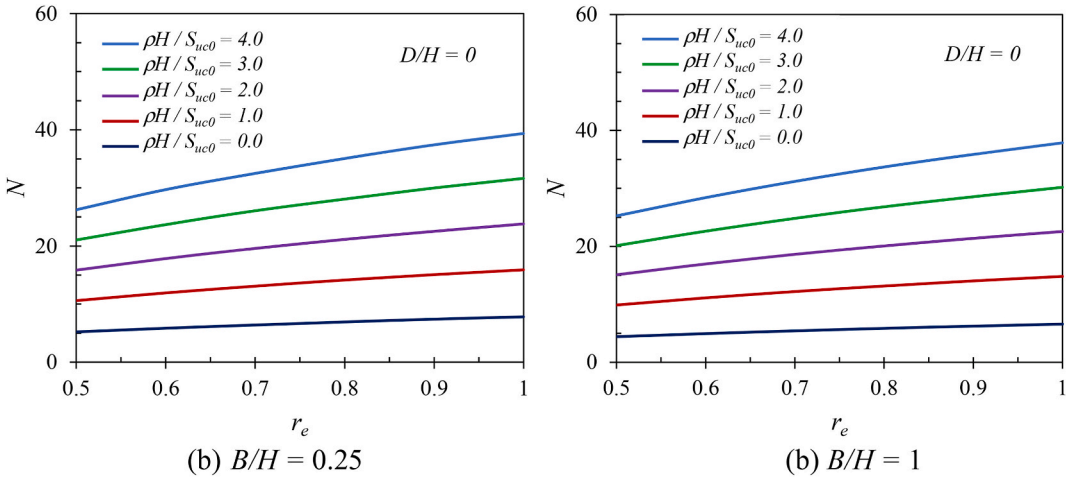

Fig. 11. Effect of the r_e on the N, where $D/H = 0$; $B/H = 0.25$, 1; $\rho H/S_{uc0} = 0$, 1, 2, 3, 4; and $r_e = 0.5$, 0.6, 0.7, 0.8, 0.9, 1.

$$RI = \frac{\sum_{m=1}^{m=N_h}\left(\left(\frac{|W_{km}^{ih}|}{\sum_{k=1}^{k=N_i}|W_{km}^{ih}|}\right)\times|W_{mn}^{ho}|\right)}{\sum_{k=1}^{k=N_i}\left\{\sum_{m=1}^{m=N_h}\left(|W_{km}^{ih}|\Big/\sum_{k=1}^{k=N_i}|W_{km}^{ih}|\right)\times|W_{mn}^{ho}|\right\}} \tag{3}$$

where x and N_x indicate the independent variables and the number of independent variables; N_h and N_i indicate the number of hidden and input neurons; W and b indicate the connection weight and bias, respectively, with the symbols *i, h,* and *o* representing the input, hidden, and output layers, respectively, and the *subscripts k, m,* and *n* representing input, hidden and output neurons, respectively.

This study selects all data from the investigated cases for use as training data. Four dimensionless investigated variables (B/H, D/H, $\rho H/S_{uc0}$, r_e), or input neurons, are adopted as independent variables, while only one target variable, N, is considered. As a result, there are 576 data sets. These data sets are randomly divided into training, validation, and testing with 70 %, 15 %, and 15 %, respectively. The optimal ANN model is selected based on using the simplest ANN model that includes one input layer, one hidden layer, and one output and considering the effect of the number of neurons in the hidden layer on the accuracy of the ANN model. The accuracy of the examined ANN model is determined through traditional regression parameters, which are the coefficient of determination (R^2) and mean squared error (MSE). The determination of MSE and R^2 can be found in Eq. (4) and Eq. (5). Fig. 17 illustrates the relationship between the number of hidden neurons and the variation in MSE and R^2, which are used to select the optimal model. Due to the increased number of hidden neurons, the R^2 is closer to 1, and the MSE is slight. When the number of hidden neurons is less than four, the values of R^2 and MSE are unstable. In contrast, R^2 and MSE stabilize when the number of hidden neurons exceeds four. These values

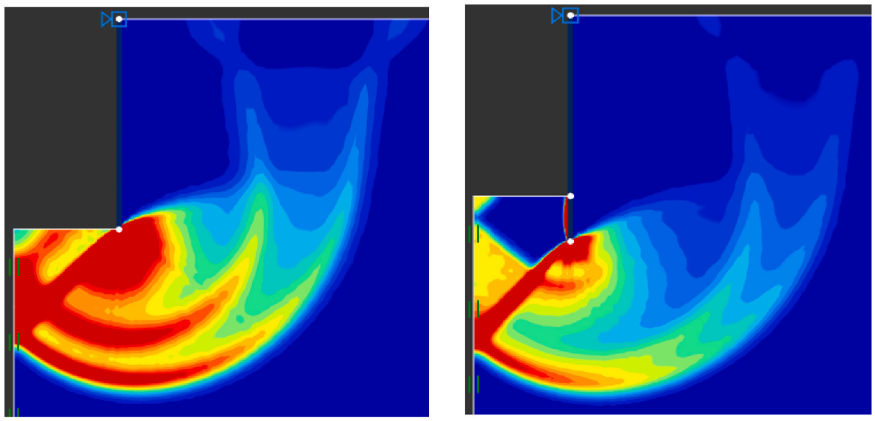

(a) $D/H = 0$ (b) $D/H = 0.25$

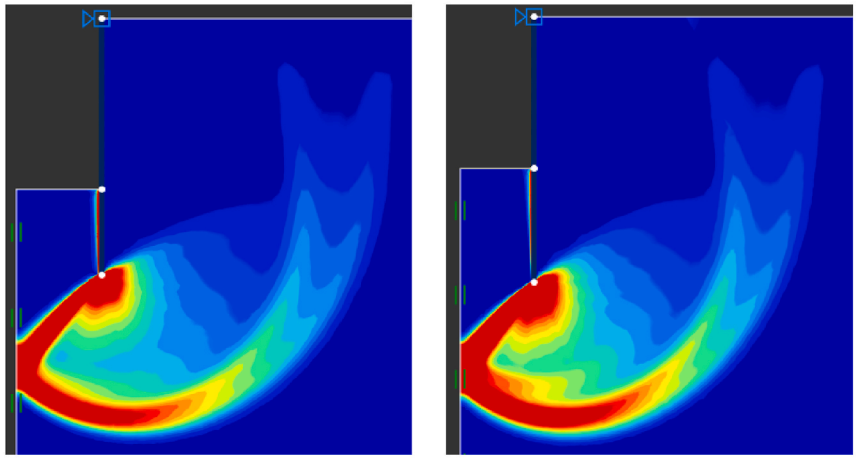

(c) $D/H = 0.50$ (d) $D/H = 0.75$

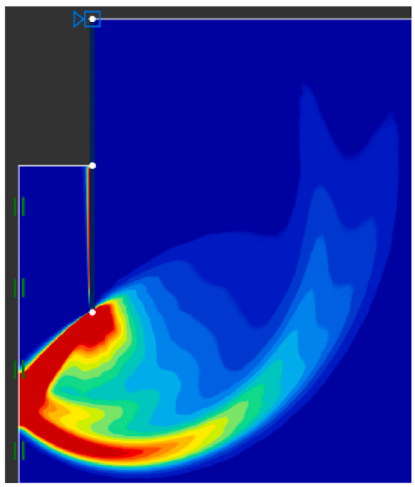

(e) $D/H = 1.0$

Fig. 12. Shear dissipation failure mechanisms of the rigid wall fully braced excavation, where $D/H = 0$, 0.25, 0.50, 0.75, and 1.0; $B/H = 1$; $r_e = 0.8$; and $\rho H/S_{uc0} = 1$.

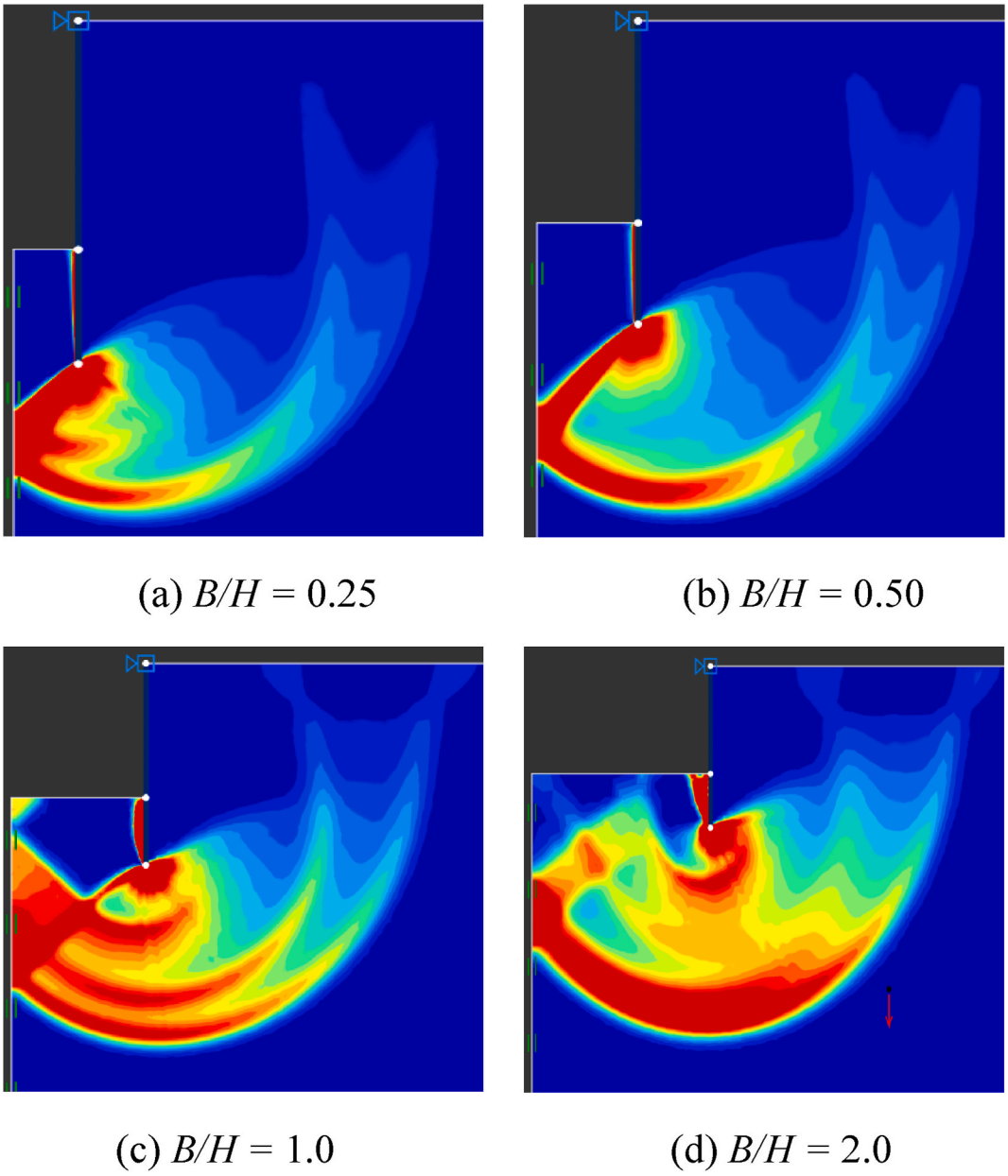

Fig. 13. Shear dissipation failure mechanisms of the rigid wall fully braced excavation, where $B/H = 0.25$, 0.50, 1, and 2; $D/H = 0.5$; $r_e = 0.8$; and $\rho H/S_{uc0} = 1$.

remain constant when the number of hidden neurons is above eight. Therefore, the simplest ANN with eight neurons in the hidden layer is chosen as the optimal model.

$$MSE = \frac{1}{n}\sum_{i=1}^{n}\left(N_i^{predict} - N_i\right)^2 \tag{4}$$

$$R^2 = 1 - \frac{\sum_{i=1}^{n}\left(N_i^{predict} - N_i\right)^2}{\sum_{i=1}^{n}\left(N_i - \overline{N}\right)^2} \tag{5}$$

where n is the number of samples and $N_i^{predict}$ and N_i indicate the predicted and input values, respectively.

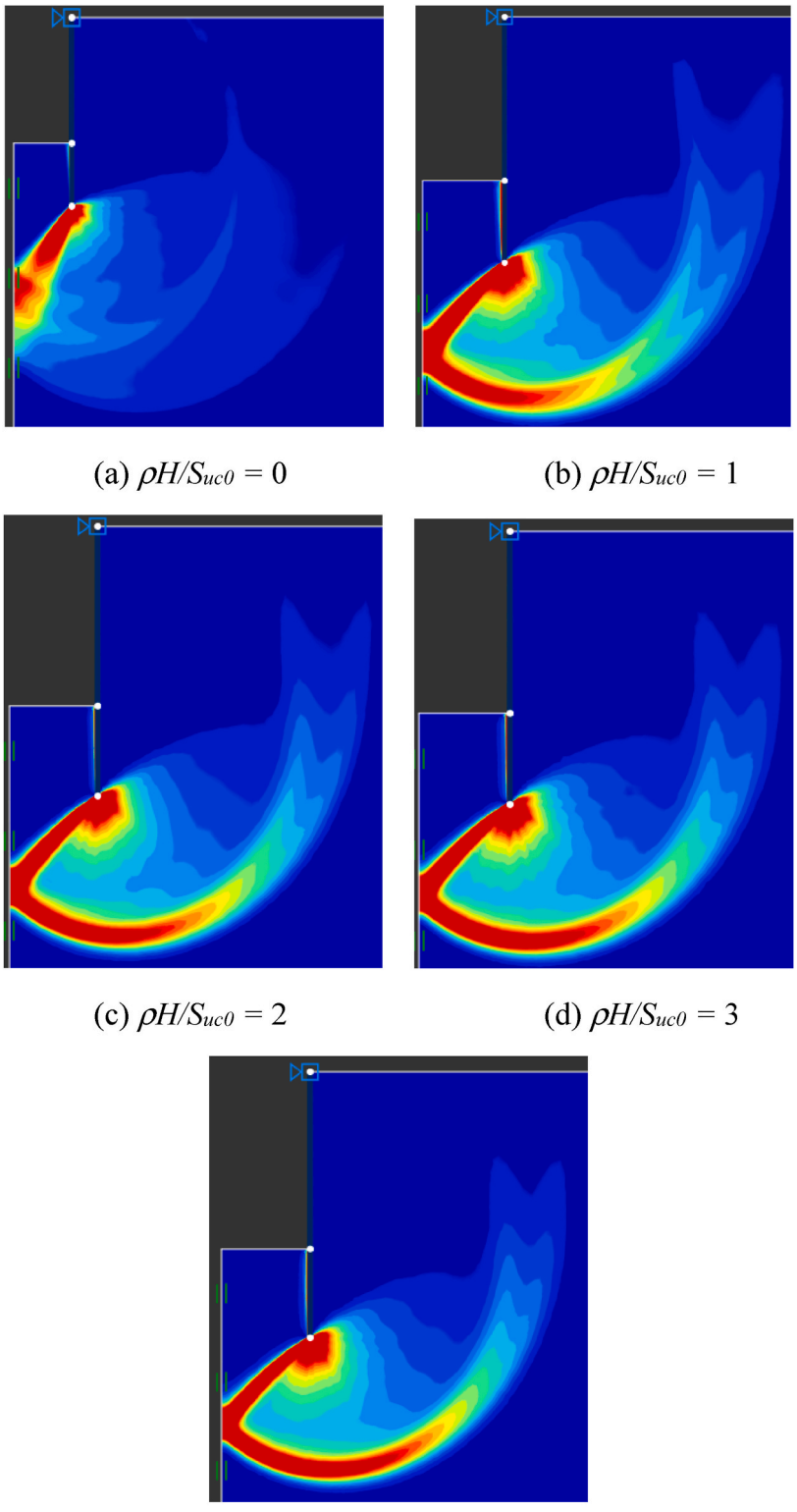

Fig. 14. Shear dissipation failure mechanisms of the rigid wall fully braced excavation, where $\rho H/S_{uc0} = 0$, 1, 2, 3, and 4; $D/H = 0.5$; $r_e = 0.8$; and $B/H = 1$.

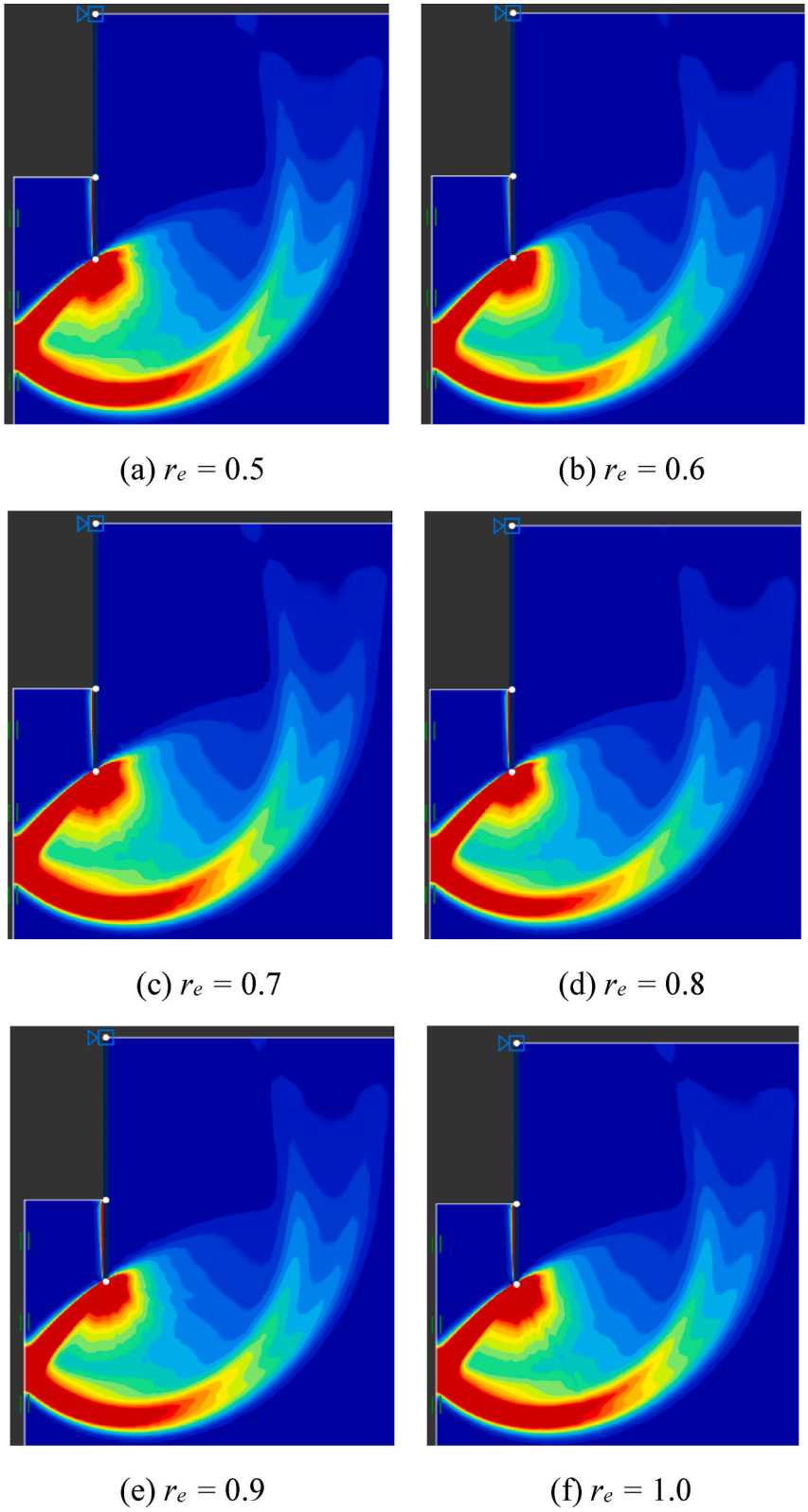

Fig. 15. Shear dissipation failure mechanisms of the rigid wall fully braced excavation, where $r_e = 0.5$, 0.6, 0.7, 0.8, 0.9, and 1; $D/H = 0.5$; $\rho H/S_{uc0} = 1$; and $B/H = 1$.

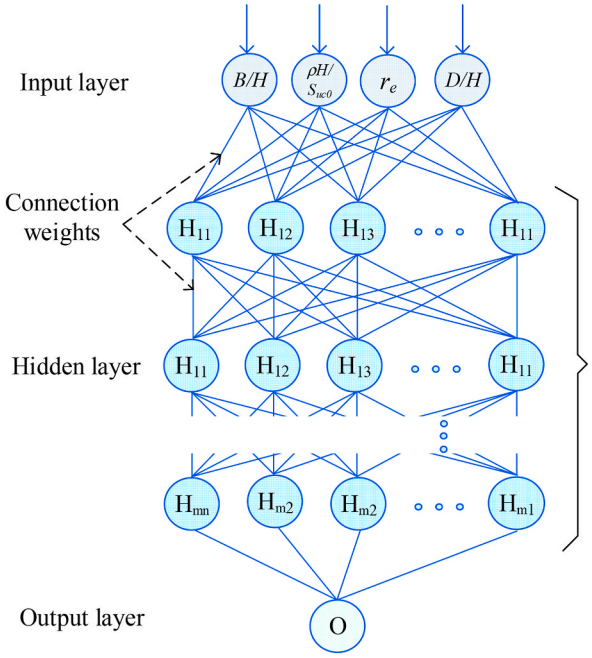

Fig. 16. Architect of general ANN model.

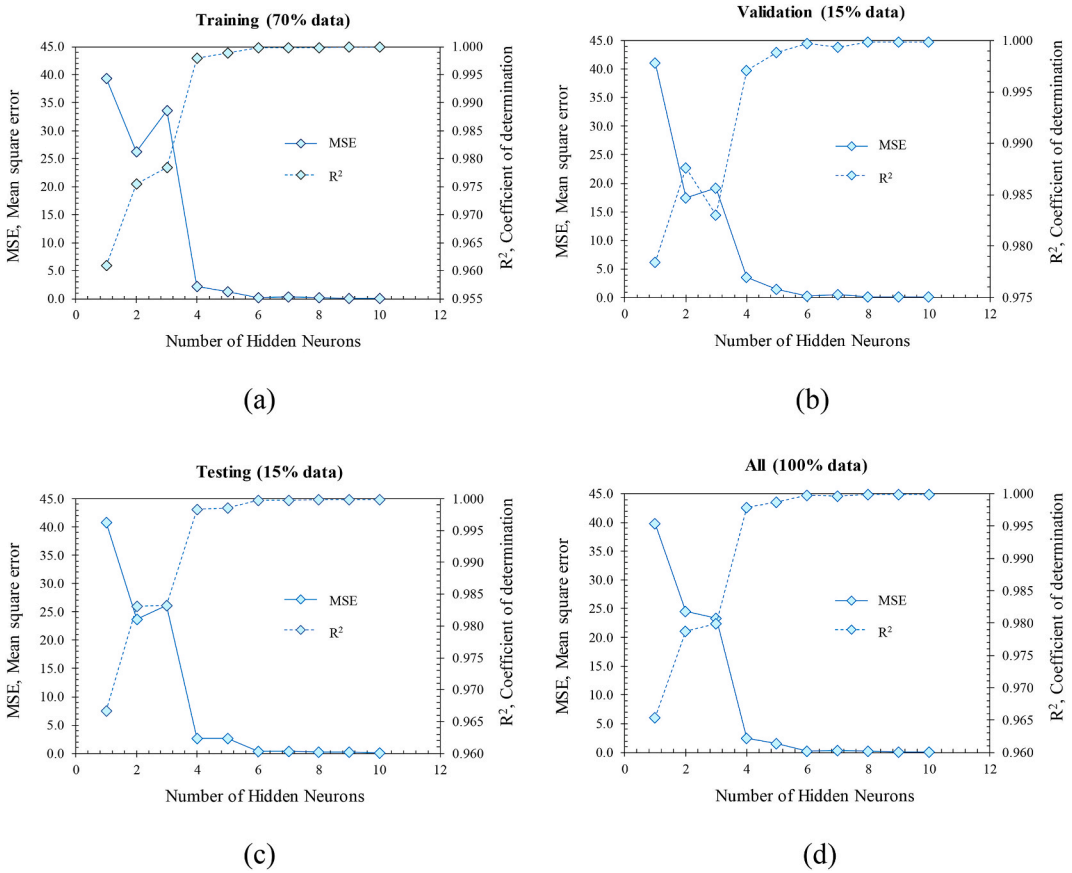

Fig. 17. Relationship between number of hidden neurons and R^2, MSE with: (a) training set (70 % data) (b) validating set (15 % data) (c) testing set (15 % data) (d) all data (100 % data).

Based on the constant values of connection weight and bias of the optimal model prepared in Table 2, the empirical equation that shows the relationship between four dimensionless investigated variables (B/H, D/H, $\rho H/S_{uc0}$, r_e) and stability number (N) is shown in Eq. (6). The empirical equation is evaluated using the numerical results presented in Fig. 18. With an R^2 of 99.98 %, the predicted stability number N is in excellent agreement with the numerical results. This result confirms that the developed empirical equation for predicting the basal heave stability number of braced excavations is a practical engineering tool.

$$N = 0.0357N_1 + 2.2905N_2 + 1.1785N_3 - 0.6486N_4 + 1.6976N_5 - 1.0330N_6 + 1.2324N_7 + 3.2987N_8 - 0.7388 \quad (6)$$

where

$$N_1 = \text{tansig}(0.6429B/H - 0.1458r_e - 1.5227\rho H/S_{uc0} + 0.8487D/H)$$

$$N_2 = \text{tansig}(-0.0448B/H + 0.0643r_e + 0.2127\rho H/S_{uc0} + 0.234D/H)$$

$$N_3 = \text{tansig}(0.0152B/H - 0.24058r_e + 0.2036\rho H/S_{uc0} + 0.1276D/H)$$

$$N_4 = \text{tansig}(0.3811B/H - 0.0292r_e + 0.4175\rho H/S_{uc0} - 0.3827D/H)$$

$$N_5 = \text{tansig}(-0.0431B/H + 0.14018r_e - 0.3051\rho H/S_{uc0}0.1447D/H)$$

$$N_6 = \text{tansig}(-1.452B/H + 0.19468r_e + 0.3218\rho H/S_{uc0} - 0.2461D/H)$$

$$N_7 = \text{tansig}(-2.2641B/H + 0.1505r_e + 0.4087\rho H/S_{uc0} + 0.374D/H)$$

$$N_8 = \text{tansig}(0.0867B/H + 0.0274r_e + 0.1726\rho H/S_{uc0} - 0.2458D/H)$$

Furthermore, the impact of each dimensionless investigated variable (i.e., B/H, D/H, $\rho H/S_{uc0}$, r_e) on the stability number is determined using Eq. (3). Moreover, sensitive results are presented in Fig. 19. According to Fig. 19, $\rho H/S_{uc0}$ is the most influential parameter with an RI of 32.96 %, followed by D/H, B/H and r_e with RIs of 27.74 %, 26.76 %, and 12.54 %, respectively. These results suit the parametric study results shown in Figs. 3, 9 and 10, where the variation between N and $\rho H/S_{uc0}$ is stronger than that between N and other parameters.

5. Conclusion

This study investigates the undrained basal stability of fully braced excavation in anisotropic clays with linearly increasing shear strength with depth employing upper and lower bound finite element limit analysis under plane strain based on the AUS failure criterion. The undrained basal stability is examined through dimensionless stability number (N) variation and the failure mechanisms due to changes in r_e, B/H, D/H, and $\rho H/S_{uc0}$. The following conclusions can be drawn from the study outcomes:

- The N factor linearly increases due to an increase in the D/H and $\rho H/S_{uc0}$ ratios and nonlinearly increases due to an increase in r_e. Conversely, the N factor decreases when the B/H ratio increases.
- The effects of D/H and B/H on shear dissipation failure mechanisms have similar formations. With a shallow embedded depth, failure occurs at the bottom of the cut, and failure occurs at the bottom of the wall in the case of a deeper embedded depth. In other ways, the failure mechanisms have small changes due to $\rho H/S_{uc0}$ and r_e variations. There occurred under the excavation zone as a spiral pattern except for a V-shaped pattern in the case of $\rho H/S_{uc0} = 0$.
- The ANN model is applied to propose an empirical equation that can serve as a valuable tool for practical engineering with an R^2 of 99.98 %. Furthermore, from the ANN model, the sensitivity results show that $\rho H/S_{uc0}$ is the most influential parameter with an RI of

Table 2
The constant weigh and bias of the selected ANN model.

Neuron	W^{ih}				b^{ih}	W^{ho}	b^{ho}
	Input variables					Output	
	B/H	r_e	$\rho H/S_{uc0}$	D/H		N	
1	0,6429	−0,1458	−1,5277	0,8487	−1,8076	0,0357	−0,7388
2	−0,0448	0,0643	0,2127	0,2340	−0,8047	2,2905	
3	0,0152	−0,2405	0,2036	0,1276	0,1267	1,1785	
4	0,3811	−0,0292	0,4175	−0,3827	0,5337	−0,6486	
5	−0,0431	0,1401	−0,3051	0,1447	0,4582	1,6976	
6	−1,4520	0,1946	0,3218	−0,2461	−3,0919	−1,0330	
7	−2,2641	0,1505	0,4087	0,3740	−3,5430	1,2324	
8	0,0867	0,0274	0,1726	−0,2458	0,4276	3,2987	

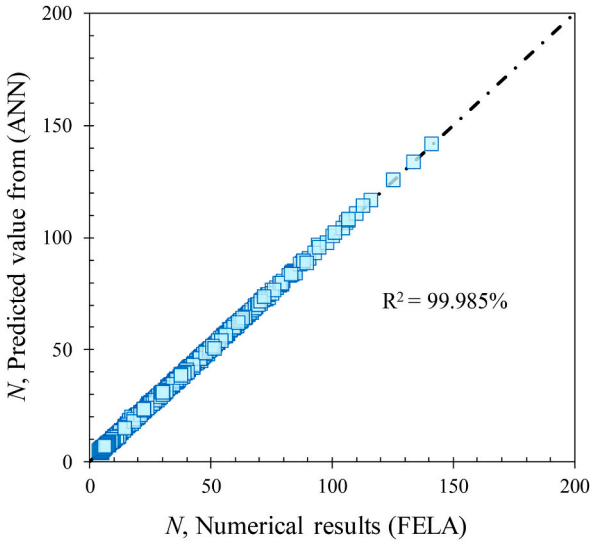

Fig. 18. Comparison between stability number for prediction and numerical results.

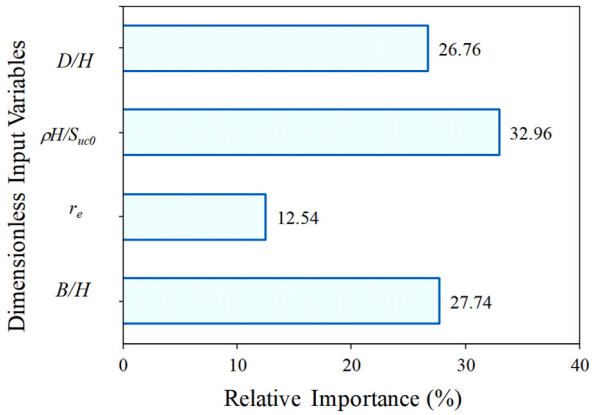

Fig. 19. Sensitivity results from ANN model.

32.96 % and that the RIs of D/H, B/H, and r_e are 27.74, 26.76, and 12.54 %, respectively, which can be used as a theoretical guideline for practical engineering in selecting parameters during the initial design process.

Data availability

Data will be made available on request.

Funding

This research was funded by National Science, Research and Innovation Fund (NSRF), and King Mongkut's University of Technology North Bangkok with Contract No. KMUTNB–FF–66–12.

CRediT authorship contribution statement

Van Qui Lai: Conceptualization, Formal analysis, Methodology, Software, Validation, Visualization, Writing – original draft. **Khamnoy Kounlavong:** Writing – original draft, Data curation, Investigation. **Suraparb Keawsawasvong:** Conceptualization, Formal analysis, Investigation, Methodology, Writing – review & editing, Funding acquisition. **Warit Wipulanusat:** Conceptualization, Formal analysis, Funding acquisition, Methodology, Software, Supervision, Writing – review & editing. **Pitthaya Jamsawang:** Conceptualization, Formal analysis, Funding acquisition, Methodology, Writing – review & editing.

Declaration of competing interest

The authors declare that they have no known competing financial interests or personal relationships that could have appeared to influence the work reported in this paper.

Acknowledgements

This work was supported by Thammasat University Research Unit in Data Science and Digital Transformation. We acknowledge Ho Chi Minh City University of Technology (HCMUT), VNU-HCM for supporting this study.

References

[1] C.C. Ladd, Stability evaluations during stage construction, J. Geotech. Eng. 117 (4) (1991) 540–615.
[2] K. Krabbenhøft, S.A. Galindo-Torres, X. Zhang, J. Krabbenhøft, AUS: anisotropic undrained shear strength model for clays, Int. J. Numer. Anal. Methods GeoMech. 43 (17) (2019) 2652–2666.
[3] S. Keawsawasvong, Bearing capacity of conical footings on clays considering combined effects of anisotropy and non–homogeneity, Ships Offshore Struct. 17 (1) (2022) 2317–2328.
[4] S. Keawsawasvong, J. Shiau, C. Ngamkhanong, V.Q. Lai, C. Thongchom, Undrained stability of ring foundations: axisymmetry, anisotropy, and non–homogeneity, Int. J. GeoMech. 22 (1) (2022), 04021253.
[5] C.N. Van, S. Keawsawasvong, D.K. Nguyen, V.Q. Lai, Machine Learning Regression Approach for Analysis of Bearing Capacity of Conical Footings in Heterogenous and Anisotropic Clay. Neural Computing and Applications, 2020. In press.
[6] D.K. Nguyen, T.P. Nguyen, C. Ngamkhanong, S. Keawsawasvong, V.Q. Lai, Bearing capacity of ring footings in anisotropic clays: FELA and ANN, Neural Comput. Appl. 35 (2023) 10975–10996.
[7] S. Keawsawasvong, K. Yoonirundorn, T. Senjuntichai, Pullout capacity factor for cylindrical suction caissons in anisotropic clays based on Anisotropic Uundrained Shear failure criterion, Transportation Infrastructure Geotechnology 8 (4) (2021) 629–644.
[8] T. Jearsiripongkul, V.Q. Lai, S. Keawsawasvong, T.S. Nguyen, C.N. Van, C. Thongchom, P. Nuaklong, Prediction of uplift capacity of cylindrical caissons in anisotropic and inhomogeneous clays using multivariate adaptive regression splines, Sustainability 14 (8) (2022) 4456.
[9] D.K. Nguyen, T.P. Nguyen, S. Keawsawasvong, V.Q. Lai, Vertical uplift capacity of circular anchors in clay by considering anisotropy and non–homogeneity, Transportation Infrastructure Geotechnology 9 (2022) 653–672.
[10] J. Shiau, V.Q. Lai, S. Keawsawasvong, Multivariate adaptive regression splines analysis for three–dimensional slope stability in anisotropic and heterogenous clay, J. Rock Mech. Geotech. Eng. (2022). In press.
[11] V.Q. Lai, J. Shiau, S. Keawsawasvong, S. Seehavong, L.T. Cabangon, Undrained stability of unsupported rectangular excavations: anisotropy and non–homogeneity in 3D, Buildings 12 (9) (2022) 142.
[12] V.Q. Lai, D.K. Nguyen, B. Banyong, S. Keawsawasvong, Limit analysis solutions for stability factor of unsupported conical slopes in clays with heterogeneity and anisotropy, International Journal of Computational Materials Science and Engineering 11 (1) (2022), 2150030.
[13] W. Yodsomjai, S. Keawsawasvong, T. Senjuntichai, Undrained stability of unsupported conical slopes in anisotropic clays based on Anisotropic Undrained Shear failure criterion, Transportation Infrastructure Geotechnology 8 (4) (2021) 557–568.
[14] V.Q. Lai, B. Banyong, S. Keawsawasvong, Stability of limiting pressure behind soil gaps in contiguous pile walls in anisotropic clays, Eng. Fail. Anal. 134 (2022), 106049.
[15] F. Lai, J. Shiau, S. Keawsawasvong, F. Chen, R. Banyong, S. Seehavong, Physics-based and data-driven modeling for stability evaluation of buried structures in natural clays, J. Rock Mech. Geotech. Eng. (2022). In pres.
[16] V.Q. Lai, R.J. Chenari, R. Banyong, S. Keawsawasvong, Undrained stability of opening in underground walls in anisotropic clays, Int. J. GeoMech. 23 (2) (2023), 06022042.
[17] M.G. Li, Z.J. Zhang, J.J. Chen, J.H. Wang, A.J. Xu, Zoned and staged construction of an underground complex in Shanghai soft clay, Tunn. Undergr. Space Technol. 67 (2017) 187–200.
[18] Z. Zhang, M. Huang, W. Wang, Evaluation of deformation response for adjacent tunnels due to soil unloading in excavation engineering, Tunn. Undergr. Space Technol. 38 (2013) 244–253.
[19] Y. Tan, D. Wang, Structural behaviours of large underground earth–retaining systems in Shanghia. I: unpropped circular diaphragm wall, J. Perform. Constr. Facil. 29 (2) (2015), 04014059.
[20] L. Mu, M. Huang, Small strain based method for predicting three–dimensional soil displacements induced by braced excavation, Tunn. Undergr. Space Technol. 52 (2016) 12–22.
[21] W. Zhang, Y. Zhang, A.T. Goh, Multivariate adaptive regression splines for inverse analysis of soil and wall properties in braced excavation, Tunn. Undergr. Space Technol. 64 (2017) 24–33.
[22] Y. Arai, O. Kusakabe, O. Murata, S. Konishi, A numerical study on ground displacement and stress during and after the installation of deep circular diaphragm walls and soil excavation, Comput. Geotech. 35 (5) (2007) 791–807.
[23] K.Y. Kim, D.S. Lee, J. Cho, S.S. Jeong, S. Lee, The effect of arching pressure on a vertical circular shaft, Tunn. Undergr. Space Technol. 37 (2013) 10–21.
[24] J. Cho, H. Lim, S. Jeong, K. Kim, Analysis of lateral earth pressure on a vertical circular shaft considering the 3D arching effect, Tunn. Undergr. Space Technol. 48 (2015) 11–19.
[25] J.L. Borges, G.T. Guerra, Cylindrical excavations in clayey soils retained by jet grout walls: numerical analysis and parametric study considering the influence of consolidation, Comput. Geotech. 55 (2014) 42–56.
[26] F.L. Peng, H.L. Wang, Y. Tan, Z.L. Xu, Y.L. Li, Field measurements and finite–element method simulation of a tunnel shaft constructed by pneumatic caisson method in Shanghai soft ground, J Geotech Geoenviron 137 (5) (2010) 516–524.
[27] G. Walton, D. Delaloye, M.S. Diederichs, Development of an elliptical fitting algorithm to improve change detection capabilities with applications for deformation monitoring in circular tunnels and shafts, Tunn. Undergr. Space Technol. 43 (2014) 336–349.
[28] Q.T. Huynh, V.Q. Lai, T. Boonyatee, S. Keawsawasvong, Verification of soil parameters of hardening soil model with small–strain stiffness for deep excavations in medium dense sand in Ho Chi Minh City, Vietnam. Innovative Infrastructure Solutions 7 (2022) 15.
[29] Q.T. Huynh, V.Q. Lai, T. Boonyatee, S. Keawsawasvong, Behavior of a deep excavation and damages on adjacent buildings: a case study in Vietnam, Transportation Infrastructure Geotechnology 8 (2021) 361–389.
[30] S. Likitlersuang, C. Chheng, S. Keawsawasvong, Structural modelling in finite element analysis of deep excavation, Journal of GeoEngineering 14 (3) (2019) 121–128.
[31] P. Guo, X. Gong, Y. Wang, H. Lin, Y. Zhao, Analysis of observed performance of a deep excavation straddled by shallowly buried pressurized pipelines and underneath traversed by planned tunnels, Tunn. Undergr. Space Technol. 132 (2023), 104946.
[32] P. Guo, X. Gong, Y. Wang, Displacement and force analyses of braced structure of deep excavation considering unsymmetrical surcharge effect, Comput. Geotech. 113 (2019), 103102.
[33] Y. Wang, J. Ouyang, P. Guo, et al., Performance of deep braced excavation under embankment surcharge load, Geotech. Geol. Eng. 41 (6) (2023) 3575–3586.
[34] P. Guo, G. Lei, L. Luo, et al., Soil creep effect on time-dependent deformation of deep braced excavation, Adv. Mater. Sci. Eng. 2022 (2022), 5655592.

[35] K. Terzaghi, Theoretical Soil Mechanics, Wiley, New York, 1943.
[36] L. Bjerrum, O. Eide, Stability of strutted excavations in clay, Geotechnique 6 (1) (1956) 32–47.
[37] A.T.C. Goh, Estimating basal heave stability for braced excavations in soft clay, J Geotech Eng 120 (8) (1994) 1430–1436.
[38] A.T.C. Goh, Deterministic and reliability assessment of basal heave stability for braced excavations with jet grout base slab, Eng. Geol. 218 (2017) 63–69.
[39] H. Faheem, F. Cai, K. Ugai, T. Hagiwara, Two–dimensional base stability of excavations in soft soils using FEM, Comput. Geotech. 30 (2) (2003) 141–163.
[40] W. Yodsomjai, V.Q. Lai, B. Banyong, V.B. Chauhan, C. Thongchom, S. Keawsawasvong, A machine learning regression approach for predicting basal heave stability of braced excavation in non–homogeneous clay, Arabian J. Geosci. 15 (2022) 873.
[41] F. Cai, K. Ugai, T. Hagiwara, Base stability of circular excavations in soft clay, J Geotech Eng 128 (8) (2002) 702–706.
[42] A.T.C. Goh, Basal heave stability of supported circular excavations in clay, Tunn. Undergr. Space Technol. 61 (2017) 145–149.
[43] S. Keawsawasvong, B. Ukritchon, Undrained basal stability of braced circular excavations in non–homogeneous clays with linear increase of strength with depth, Comput. Geotech. 115 (2019), 103180.
[44] R. Zhang, A.T.C. Goh, Y. Li, et al., A simple estimation model for basal heave stability of braced excavations in anisotropic clay, Acta Geotech 17 (2022) 5789–5800.
[45] R. Zhang, A.T.C. Goh, Y. Li, et al., Assessment of apparent earth pressure for braced excavations in anisotropic clay, Acta Geotech 16 (2021) 1615–1626.
[46] V.Q. Lai, K. Kounlavong, S. Keawsawasvong, R. Banyong, W. Wipulanusat, P. Jamsawang, Undrained basal stability of braced circular excavations in anisotropic and non-homogeneous clays, Transportation Geotechnics 39 (2023), 100945.
[47] OptumCE OptumG2. Copenhagen, Denmark: Optum Computational Engineering. See https://optumce.com/. Accessed 1 December 2020..
[48] C. Ngamkhanong, S. Keawsawasvong, T. Jearsiripongkul, et al., Data-Driven prediction of stability of rock tunnel heading: an application of machine learning models, Infrastructure 7 (11) (2022) 148.
[49] Q.T. Nguyen, R. Livaoglu, Combination of an inverse solution and an ANN for damage identification on high-rise buildings, Smart Struct. Syst. 28 (3) (2021) 375–390.
[50] P. Goodarzizad, E. Mohammadi Golafshani, M. Arashpour, Predicting the construction labour productivity using artificial neural network and grasshopper optimisation algorithm, International Journal of Construction Management (2021) 1–17.
[51] M. Mohseni-Dargah, Z. Falahati, B. Dabirmanesh, P. Nasrollahi, K. Khajeh, Machine learning in surface plasmon resonance for environmental monitoring, in: Artificial Intelligence and Data Science in Environmental Sensing, Academic Press, 2022, pp. 269–298.
[52] W. Zhang, X. Gu, L. Hong, L. Han, L. Wang, Comprehensive review of machine learning in geotechnical reliability analysis: algorithms, applications and further challenges, Appl. Soft Comput. 136 (2023), 110066.
[53] W. Zhang, H. Li, L. Tang, et al., Displacement prediction of Jiuxianping landslide using gated recurrent unit (GRU) networks, Acta Geotech 17 (2022) 1367–1382.
[54] S. Liu, L. Wang, W. Zhang, et al., A physics-informed data-driven model for landslide susceptibility assessment in the Three Gorges Reservoir Area, Geosci. Front. 14 (2023), 101621.
[55] K.K. Phoon, W. Zhang, Future of machine learning in geotechnics, Georisk (2022), https://doi.org/10.1080/17499518.2022.2087884.
[56] W. Zhang, X. Gu, L. Tang, et al., Application of machine learning, deep learning and optimization algorithms in geoengineering and geoscience: comprehensive review and future challenge, Gondwana Res. 109 (2022) 1–17.
[57] J. Chen, H. Huang, A.G. Cohn, D. Zhang, M. Zhou, Machine learning-based classification of rock discontinuity trace: SMOTE oversampling integrated with GBT ensemble learning, Int. J. Min. Sci. Technol. 32 (2) (2022) 309–322.
[58] D.K. Nguyen, T.P. Nguyen, C. Ngamkhanong, S. Keawsawasvong, T.K. Nguyen, V.Q. Lai, Prediction of uplift resistance of circular anchors in anisotropic clays using MLR, ANN, and MARS, Appiled Ocean Research 136 (2023), 103584.
[59] V.Q. Lai, M.N. Tran, J. Shiau, S. Keawsawasvong, B.V. Le, T.K. Nguyen, B.Q. Le, Uplift resistance of caisson foundation in NGI-ADP soil using FEA and ANN, Adv. Eng. Software 184 (2023), 103513.
[60] W. Jitchaijaroen, W. Wipulanusat, S. Keawsawasvong, J. Chavda, S. Ramjan, J. Sunkpho, Stability evaluation of elliptical tunnels in natural clays by integrating FELA and ANN, Results in Engineering 19 (2023), 101280.
[61] S. Panomchaivath, W. Jitchaijaroen, B. Banyong, S. Keawsawasvong, S. Sirimontree, P. Jamsawang, Prediction of undrained lateral capacity of free-head rectangular pile in clay using finite element limit analysis and artificial neural network, Engineered Science (2023), https://doi.org/10.30919/es923.
[62] K. Kounlavong, J. Shiau, V.Q. Lai, V.B. Chauhan, P. Jamsawang, S. Keawsawasvong, Data-driven modeling for stability evaluation of cylindrical boreholes with slurry in anisotropic and non-homogeneous clays, Engineered Science (2023), https://doi.org/10.30919/es921.
[63] V.Q. Lai, K. Kounlavong, S. Keawsawasvong, J.T. Chavda, P. Jamsawang, Stability analysis of buried pipelines under combined uplift and lateral forces using FELA and ANN, Appiled Ocean Research 135 (2023), 103568.
[64] V.Q. Lai, W. Jitchaijaroen, S. Keawsawasvong, J. Chavda, W. Sae-Long, S. Limkatanyu, Application of ANN and FELA for predicting bearing capacity of shell foundations on sand, Int. J. Geosynth. Ground Eng. 9 (2023) 18.
[65] V.Q. Lai, J. Shiau, C.N. Van, H.D. Tran, S. Keawsawasvong, Bearing capacity of conical footing on anisotropic and heterogeneous clays using FEA and ANN, Mar. Georesour. Geotechnol. (2022).
[66] T. Jearsiripongkul, S. Keawsawasvong, C. Thongchom, C. Ngamkhanong, Prediction of the stability of various tunnel shapes based on Hoek-Brown failure criterion using artificial neural network (ANN), Sustainability 14 (8) (2022) 4533.
[67] S. Keawsawasvong, S. Seehavong, C. Ngamkhanong, Application of artificial neural networks for predicting the stability of rectangular tunnel in Hoek-Brown rock masses, Front. Eng. Built Environ. 8 (2022), 837745.